



HAL
open science

Stochastic characterization of textile reinforcements in composites based on X-ray microtomographic scans

Anna Madra, Philippe Causse, François Trochu, Jérôme Adrien, Éric Maire, Piotr Breilkopf

► **To cite this version:**

Anna Madra, Philippe Causse, François Trochu, Jérôme Adrien, Éric Maire, et al.. Stochastic characterization of textile reinforcements in composites based on X-ray microtomographic scans. *Composite Structures*, 2019, 224, pp.111031. 10.1016/j.compstruct.2019.111031 . hal-02271609

HAL Id: hal-02271609

<https://hal.science/hal-02271609>

Submitted on 12 Sep 2022

HAL is a multi-disciplinary open access archive for the deposit and dissemination of scientific research documents, whether they are published or not. The documents may come from teaching and research institutions in France or abroad, or from public or private research centers.

L'archive ouverte pluridisciplinaire **HAL**, est destinée au dépôt et à la diffusion de documents scientifiques de niveau recherche, publiés ou non, émanant des établissements d'enseignement et de recherche français ou étrangers, des laboratoires publics ou privés.

Stochastic characterization of textile reinforcements in composites based on X-ray microtomographic scans

Anna Madra^{a,*}, Philippe Causse^b, François Trochu^b, Jérôme Adrien^c, Eric Maire^c, Piotr Bretkopf^d

^a Department of Civil and Environmental Engineering, The Pennsylvania State University, State College 16802, PA, USA

^b Department of Mechanical Engineering, Research Center for High Performance Polymer and Composite Systems, École Polytechnique de Montréal, Montréal H3C 3A7, Canada

^c Université de Lyon, INSA-Lyon, MATEIS CNRS UMR5510, 7 Avenue Jean Capelle, 69621 Villeurbanne, France

^d Laboratoire Roberval, FRE UTC-CNRS 2012, Sorbonne Universités, Université de Technologie de Compiègne, Centre de Recherches de Royallieu, 60319 Compiègne, France

ARTICLE INFO

Keywords:

Textile composites
X-ray microtomography
Multi-scale modeling
Uncertainty quantification

ABSTRACT

A stochastic method is introduced to characterize the dual-scale geometry of textile reinforcements in composites. The fiber tows are identified automatically from X-ray microtomographic scans with a machine learning algorithm, quantifying the error of the procedure. The tow geometry is then used to construct a stochastic model as a Gaussian Random Process which permits quantification of the uncertainty in the measurements of micro-scale fiber volume fraction. The hyperparameters of the model are calibrated with a custom-built multi-objective evolutionary algorithm. The approach is illustrated by the analysis of a vinyl-ester composite reinforced with a glass fiber non-crimp fabric.

1. Introduction

Recently, with the advances in hardware, the capacity to simulate the mechanical behavior or manufacturing processes of complex materials such as composites, has increased considerably [1–7]. Given such possibilities, the researchers turn to models closely connected to the experimental microstructure of materials. One example is the simulation of Liquid Composite Molding (LCM) where a liquid polymer resin is injected through a fibrous reinforcement. Engineering textiles, commonly used in high-performance composites [8,9], consist of fiber tows which in turn are bundles of fiber filaments. This results in a dual-scale architecture with individual fibers at microscale and fiber tow at mesoscale. As the impregnation behavior strongly depends on the geometry of the reinforcement [10], a realistic model of the mesoscale geometry together with a microscale fiber volume fraction is required.

Volume imaging techniques such as X-ray microtomography can be used to retrieve the realistic geometry of fibrous reinforcement in composites [11,12,5]. To achieve this, a segmentation process is performed to partition the scans (Fig. 1a) into phase- (Fig. 1b) or structure-specific (Fig. 1c) regions. Existing approaches range from manual fitting of shapes [9], through simple algorithms such as thresholding [13–15] to machine learning solutions [16]. While segmentation of phases is quite consistent, especially in materials science, where the phase-

specific coefficient of attenuation μ is relatively constant, the same is not true for structure segmentation. The identification of structures, i.e., spatial conglomerates of phases, requires a more comprehensive approach than in case of phases. In the latter, the intensity of μ is a sufficient feature to obtain plausible results [17,18,9], although the presence of imaging-related artifacts may contribute to the overall error of further measurements. In case of structures, the μ may not be enough to perform the segmentation, since spatial conglomerates such as fiber tows may consist of multiple phases, including polymer matrix and residual voids trapped between individual fibers. Thus an approach that takes into account the underlying geometry of the tows has to be employed.

Additional problem is the ambiguity in the definition of fiber tow geometry. A tow cross-section should be a closed curve that encompasses the smallest area containing all of the individual fibers comprising the tow. At the same time, the perimeter of the cross-section should be the smallest possible, striving towards a compact geometry, permitting accurate measurements of the local fiber volume fraction V_f . To our best knowledge, none, if any research in computational material science has addressed the problem of quantification of the two sources of error: structure segmentation algorithm and the ambiguity of tow geometry definition. Most of the segmentation methods are dedicated to maximizing the compliance with “ground truth”, namely the manual

* Corresponding author.

E-mail address: annamadra@psu.edu (A. Madra).

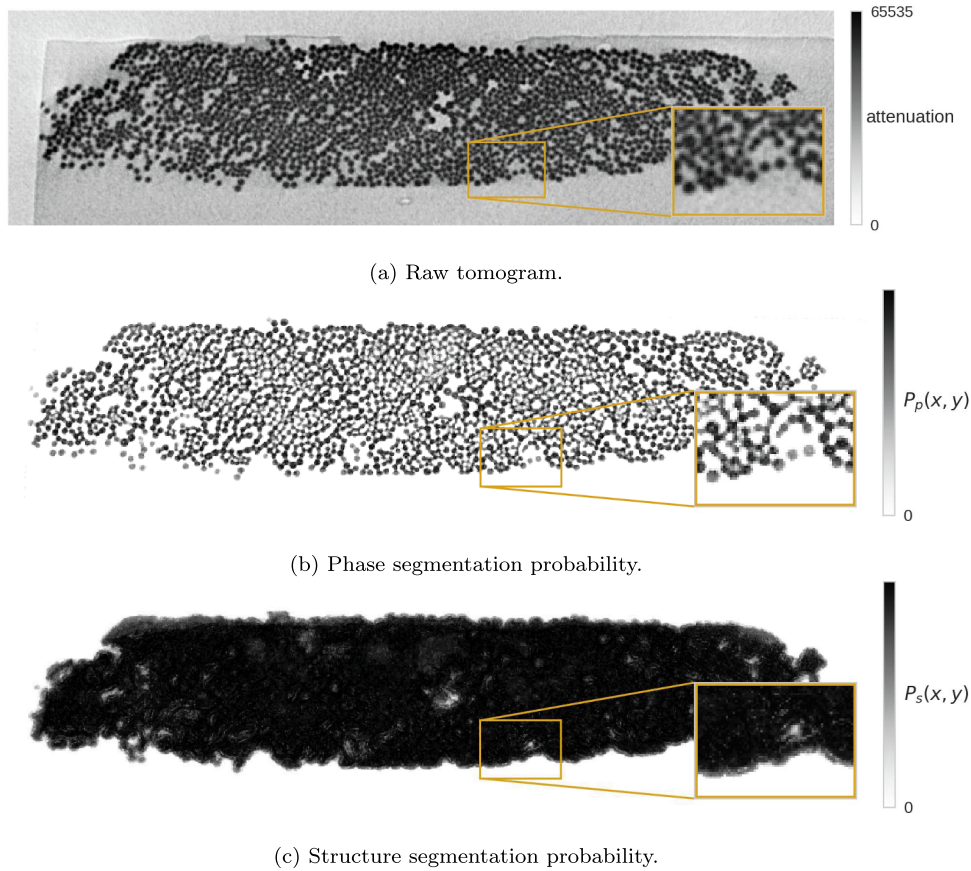


Fig. 1. Results of the X-ray micro-tomographic scan of a polymer composite with glass fiber reinforcement TG96N60E from *Texonic*: (a) raw, unprocessed tomogram; (b) phase segmentation probability; (c) structure segmentation probability.

segmentation provided by a human expert. The workload involved in performing manual segmentations is substantial, hence the spectrum of possible results is not thoroughly analyzed. However, in the medical domain, Lê et al. [19] performed the identification of tumor tissue from X-ray tomographic scans by modeling the tumor boundary with level sets. A Gaussian Random Process (GRP) was then used to generate new partitions. Based on the position and area of the generated samples, the amount of radiation required to eradicate the tumor was estimated. Level sets were also used in [20] to obtain a unique segmentation of brain tissues, where the probability of the generated level set contours was described by a multivariate Gaussian distribution, and the contour with the highest likelihood was ultimately chosen. Finally, a unique segmentation of coronary arteries was obtained in [21] after sampling thresholds for image filtering and using multi-objective optimization with genetic algorithms to select the most plausible one.

In material studies, the results of segmentation in X-ray micro-tomography are usually not subject to error estimation, only sometimes accompanied by sensibility studies [22]. In [16], we have proposed a segmentation method based on dual kriging for identifying fiber tows in composite reinforcements. However, the kriging approximation, despite the availability of the error estimator σ , still provides deterministic results.

In the present work, we focus on constructing a model based on the actual microstructure while taking into account the measurement error and controlling the level of simplification. The kriging model is extended by making use of the structure of the underlying Gaussian Process to automatically generate new, plausible segmentations by affine transformation of independent multivariate Gaussian samples in a Monte Carlo manner [23]. This approach enables us to characterize the probability distribution of material properties, such as fiber tow volume or microscale fiber volume fraction. The ultimate goal is the uncertainty

quantification and propagation across the simulation of resin injection during manufacture.

The rest of this paper is organized as follows. In Section 2 we formulate the conditional GRP distribution of a fiber tow contour that is then applied in Section 3 to generate a range of admissible contours for which a specific material parameter can be calculated, and its probabilistic distribution examined. The model is calibrated in Section 4 by choosing an adequate kernel function with hyperparameters optimized taking into account the geometric metrics of the structure. The metrics are formulated as objective functions and subject to multi-objective optimization. The approach is tested in Section 5 to identify glass fiber volume fraction of a typical composite specimen manufactured by Resin Transfer Molding (RTM).

2. Stochastic model of a fiber tow geometry

Two levels of segmentation are considered in this work: the phase segmentation determining the distribution ϕ of individual fibers and the structure segmentation identifying the geometry of fiber tows. The ϕ is defined based on the probability of phase segmentation $P_p(x, y)$ (Fig. 1c)

$$\phi(x, y) = \begin{cases} 1, & \text{if } P_p(x, y) \geq d_t \\ 0, & \text{otherwise} \end{cases} \quad (1)$$

where d_t is an empirically determined threshold value. The cross-section Ω of a tow grouping individual fibers is obtained with structural segmentation (Fig. 1c) that yields probability $P_s(x, y)$ from which a contour Γ is identified with an error. Γ is expressed in a parametric form with $x(t)$, $y(t)$ as functions of a curvilinear coordinate t . We represent $X(t)$ by a Gaussian Random Process \mathcal{GP}

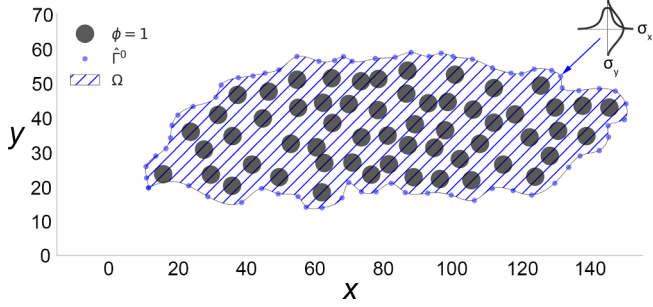


Fig. 2. Points (x^0, y^0) defining contour $\hat{\Gamma}^0$ of section Ω identified during tow segmentation superimposed on the function $\phi(x, y)$ of material distribution.

$$(X(t))_{t \in (0,1)} \sim \mathcal{GP}(\mu_x, k_x) \quad (2)$$

where μ_x is a mean function

$$\mu_x(t) = p^T(t)\beta_x \quad (3)$$

with β_x denoting a vector of coefficients of polynomial basis and k_x is a covariance function. Similarly

$$(Y(t))_{t \in (0,1)} \sim \mathcal{GP}(\mu_y, k_y). \quad (4)$$

We assume that a discrete instance of \mathcal{GP} at n_t^* sample points t^* follows a multivariate Gaussian distribution

$$(X^*|X(t^0) = x^0) \sim \mathcal{N}(m_x, K) \quad (5)$$

conditioned by observed values $x_i^0, y_i^0, i = 1, \dots, n_t^0$ of a tow contour $\hat{\Gamma}^0$ (Fig. 2) associated with the measurement error variance $\sigma^2(t_i^0)$ at discrete points $t^0 = [t_1^0, \dots, t_{n_t^0}^0]$. The Gaussian regression [24] yields the conditional mean vector m_x of length n_t^*

$$m_x = \mu^* + C^{*0}(C^{00})^{-1}(x^0 - \mu^0) \quad (6)$$

and a conditional covariance matrix K of dimensions $n_t^* \times n_t^*$

$$K = C^{**} - C^{*0}(C^{00})^{-1}C^{0*} \quad (7)$$

where

$$C_{ij}^{00} = k(t_i^0, t_j^0) + \alpha \sigma^2(t_i^0) \delta_{ij}, \quad i, j = 1, \dots, n_t^0, C_{ij}^{0*} = k(t_i^0, t_j^*), \quad i = 1, \dots, n_t^0, \\ j = 1, \dots, n_t^* C_{ij}^{**} = k(t_i^*, t_j^*), \quad i, j = 1, \dots, n_t^*. \quad (8)$$

Parameter α allows to scale the contribution of the segmentation error and δ_{ij} is the Kronecker delta (no summation over i). Furthermore, μ_x is defined as

$$\mu_x = (\mu_x^* \mu_x^0, \mu_{x_i}^* \mu_{x_i}^0) = p^T(t_i^*)\beta_x, \quad i = 1, \dots, n_t^*, \mu_{x_i}^0 = p^T(t_i^0)\beta_x, \quad i = 1, \dots, n_t^0 \quad (9)$$

with β fitted by Least Squares Fitting. The means m_x and m_y (obtained in an analogous manner) represent the kriging approximation of the contour Γ . The variance of the estimation is given by diagonal terms of matrix K

$$\sigma_i^2 = K_{ii}, \quad i = 1, \dots, n_t^*. \quad (10)$$

Considering a closed contour Γ , we propose a periodic exponential squared kernel function

$$k(t_i, t_j) = \exp^2\left(-\frac{1}{\theta} \sin^2(\pi(t_i - t_j))\right), \quad \theta \in (0, 1) \quad (11)$$

with a single length-scale hyperparameter θ . Example kernels are shown in Fig. 3 for $t_i = 0, \dots, 1$ and varying θ . The value of θ governs the size of the domain of influence. For $\theta = 1$ every point contributes equally leading to overfitting, especially for low values of α (Fig. 4a), which result in interpolation. Less accurate approximations are obtained for low values of θ , e.g., $\theta = 0.01$ and $\theta = 0.1$ which together with the increase in α lead to smoother, elliptical contours (Fig. 4b). The zone of influence of θ depends also on the density of data coordinates, with sparse values leading to more variability in the reconstruction.

3. Stochastic sampling

As stated in the introduction, the \mathcal{GP} mean vectors m_x and m_y provide a deterministic approximation of the contour. Here, we take advantage of the formulation of the model as a Gaussian Process to investigate the probability distributions of physical quantities. Namely, we can generate new, plausible contour samples

$$\hat{\Gamma}(t^*) \sim \mathcal{N}(m_x, K) \quad (12)$$

through an affine transformation

$$x^* = m_x(t^*) + Au \quad (13)$$

of independent multivariate samples u taken from

$$U \sim \mathcal{N}(0, I) \quad (14)$$

where A is determined from Cholesky's decomposition of K

$$K = AA^T. \quad (15)$$

This decomposition has to be performed only once and then A can be used to generate new contours at the cost of a single matrix-vector multiplication. The examples of such contours are shown in Fig. 5. The scaling factor α (Eq. (8)) permits to control the influence of the segmentation error on the approximation of the contour. In Fig. 5a, the error is scaled with a coefficient $\alpha = 0.05$, yielding both mean and samples with low variability, almost interpolating data. Increasing α is effective when a calibration of the segmentation is required as it enables exploration of contours that are dissimilar from the initial data. The smaller values of α are useful in estimating material properties from the model that is already calibrated. This strategy is summarized in Alg. 1 and will be now applied to process experimental microtomographic data.

Algorithm 1: Generation of new contours by sampling of the calibrated \mathcal{GP} model.

Input	: m_x, m_y, K_x, K_y
Parameters	: number of samples S
1	calculate A_x, A_y (Eq. 15);
2	for 1 to S do
3	get a random sample u from $\mathcal{N}(0, I)$ (Eq. 14);
4	calculate (x^*, y^*) from Eq. 13
5	end
6	return the set of samples $\hat{\Gamma}^*$;

4. Kernel calibration

The kernel k modeling covariance C in Eq. (8) is calibrated by adjusting the hyperparameter θ . The choice of θ is directed by the physical plausibility of the model, i.e., how well it approximates the geometry of the fiber tow. We assume that:

- the number of fibers in a fiber tow is constant,
- the diameter of each individual fiber is constant,

implying that the total area vol_{fib} of fibers at each section orthogonal to the centroid line of the fiber tow is also constant. As the sections in question are the volumes of thickness Δz and are represented by voxels, the term "fiber volume" is more appropriate. The measurement of vol_{fib} from a microtomographic scan is further detailed in [16]. The following functions need to be considered

$$f_1(\theta) = \left| vol_{fib} - \Delta z \int_{\Omega(\theta)} \phi(x, y) d\Omega(\theta) \right| f_2(\theta) \\ = \int_0^1 \sqrt{\left(\frac{dm_x(t, \theta)}{dt} \right)^2 + \left(\frac{dm_y(t, \theta)}{dt} \right)^2} dt f_3(\theta) \\ = \frac{1}{2} \int_0^1 \left(m_x(t, \theta) \frac{dm_y(t, \theta)}{dt} - m_y(t, \theta) \frac{dm_x(t, \theta)}{dt} \right) dt. \quad (16)$$

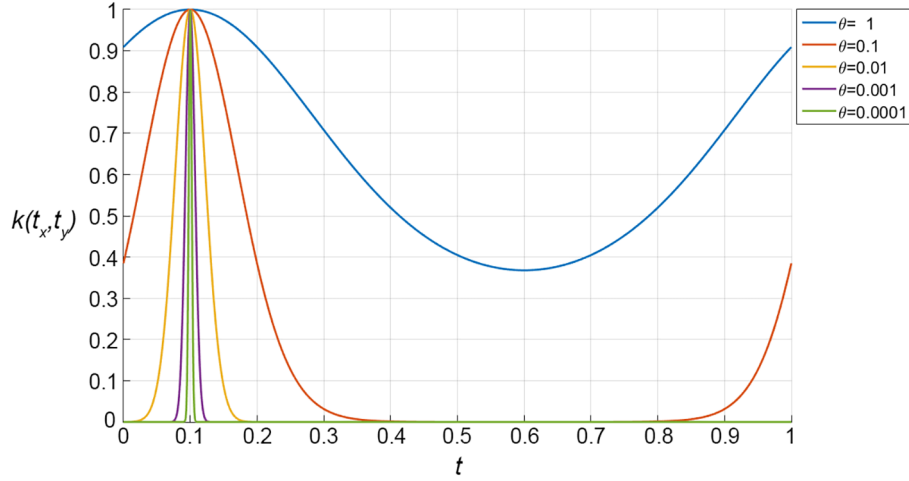


Fig. 3. Shape of kernel function defined in Eq. (11) for $t_i = 0, \dots, 1$ and for varying θ (length-scale).

Function f_1 measures the difference between vol_{fib} and the total fiber surface within the approximated contour; f_2 is the contour length and f_3 the area of the contour.

We can thus formulate a bi-objective optimization problem

$$\begin{cases} \Theta = \text{Arg min}(f_2(\theta), f_3(\theta)) \\ f_1(\theta) \leq \varepsilon \\ 0 \leq \theta \leq 1 \end{cases} \quad (17)$$

where f_2, f_3 are objective functions and f_1 is an inequality constraint which restricts the admissibility of the generated contour (Fig. 6) to the domains containing the required volume of fibers vol_{fib} . Simultaneous minimization of f_2 and f_3 imposes a specific character on the reconstructed geometry by a compromise between minimal contour length (f_2) and minimal volume (f_3). As observed in Fig. 7, the objective functions are nonlinear in θ and exhibit multiple local minima. Thus, the optimization is performed by an evolutionary algorithm inspired by the Non-dominated Sorting Genetic Algorithm II (NSGA-II) by Deb

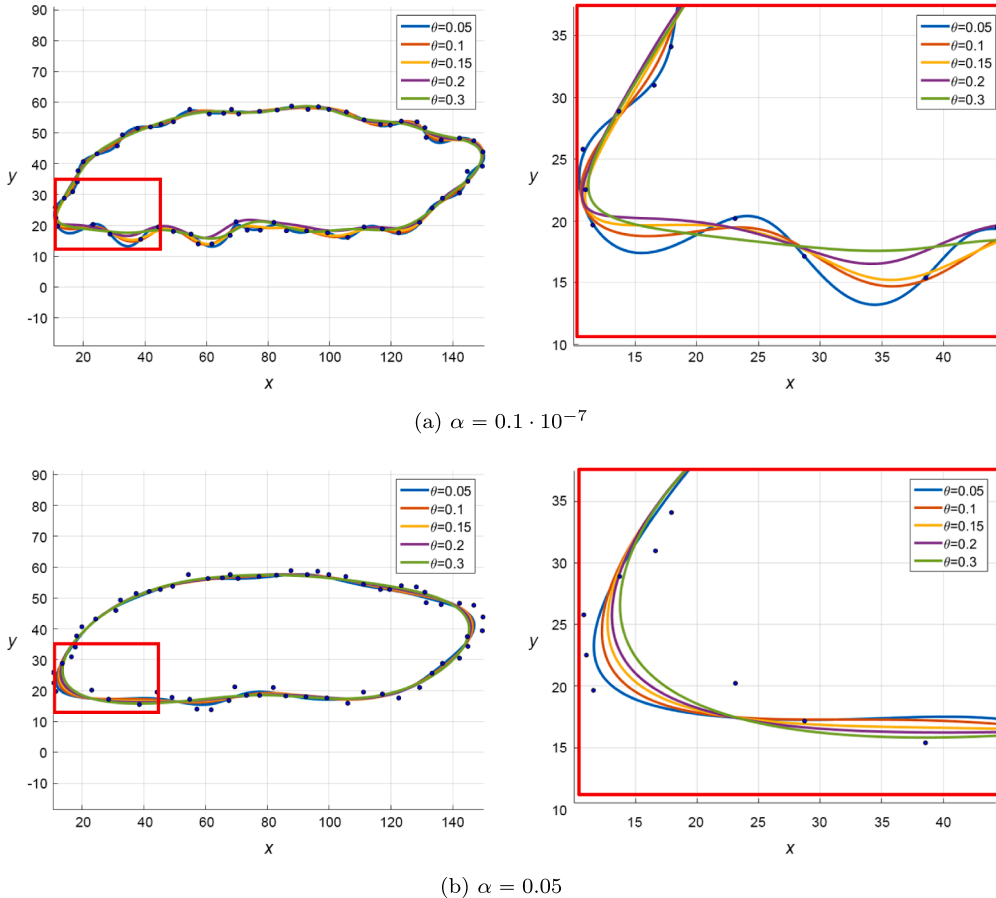


Fig. 4. Mean (m_x, m_y) (Eq. (6)) of the Gaussian Process for different values of θ and α : (a) $\alpha = 0.1 \cdot 10^{-7}$; (b) $\alpha = 0.05$.

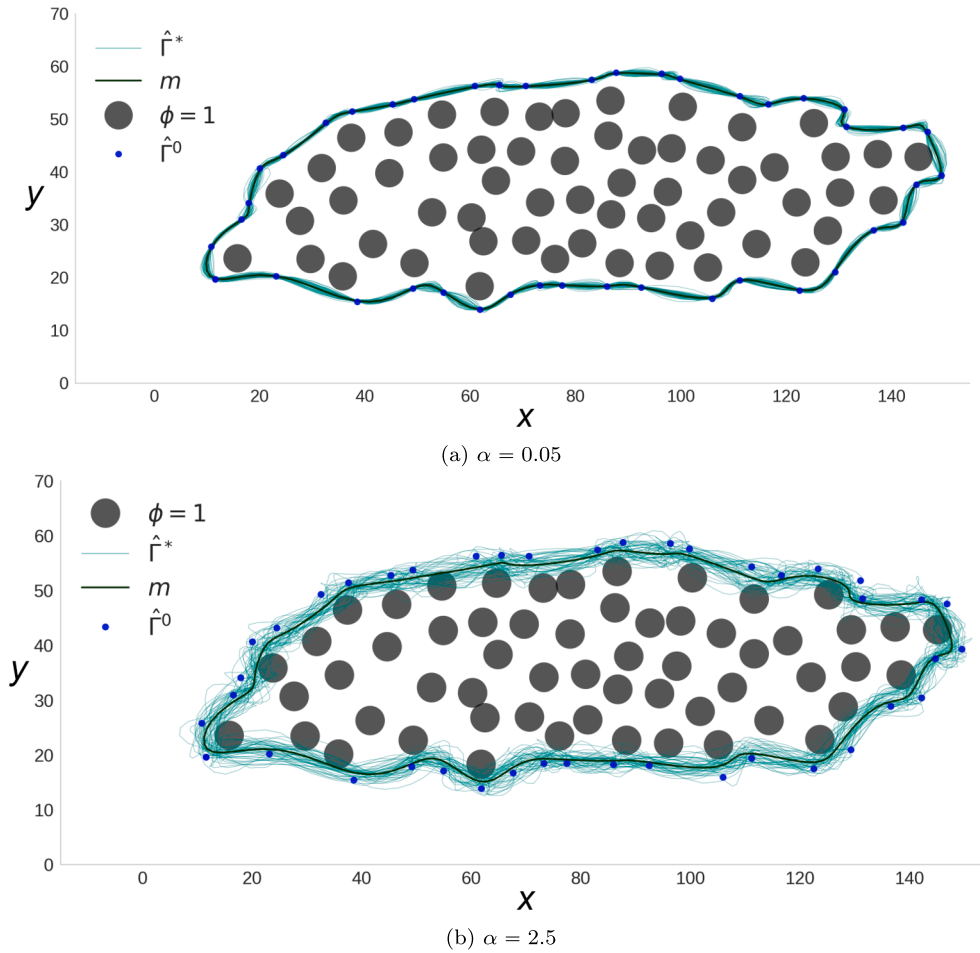


Fig. 5. Mean and samples of the contour $\hat{\Gamma}$ modeled with a Gaussian Process with different values of error scaling factor α : (a) $\alpha = 0.05$; (b) $\alpha = 2.5$.

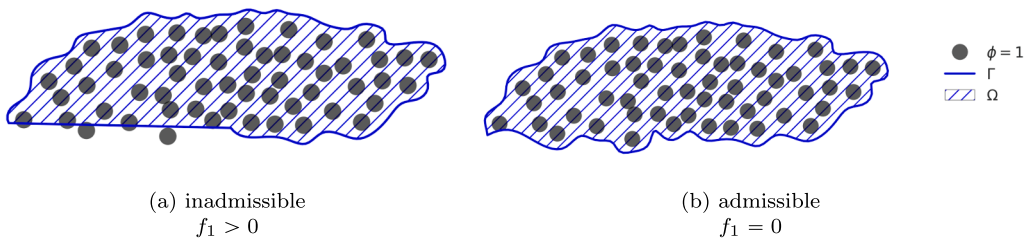


Fig. 6. Admissibility of contour $\hat{\Gamma}$ based on f_1 .

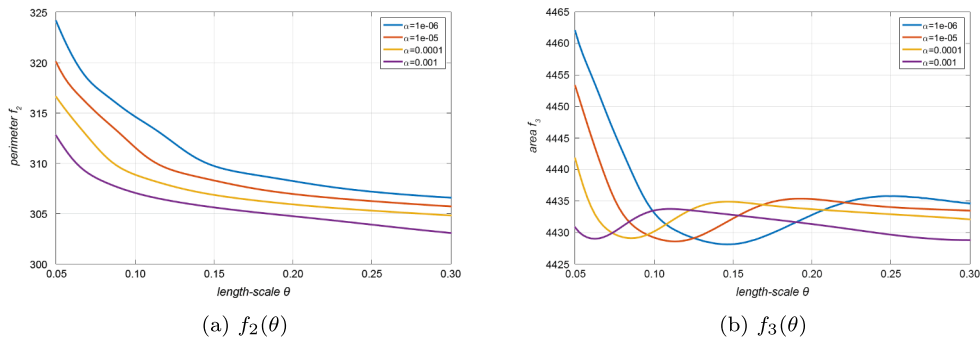


Fig. 7. Values of (a) f_2 (contour perimeter) and (b) f_3 (tong area) in function of θ (length-scale).

[25]. The algorithm is described in Appendix A.

5. Test case: fiber volume fraction of a textile composite

So far, the methodology has been illustrated with abstract cases of simplified fiber tow geometry. Here, we present how the stochastic model performs on the actual microtomographic data. In addition to the exploration of various types of reconstructions, we present an application of the stochastic formulation to characterize the fiber volume fraction V_f of a fiber tow. The approach will follow the steps outlined in Program 1. The phase and structure segmentation of raw tomograms are performed following the procedures in [16] and further data preprocessing step is performed as described in Section 5.2. The microtomographic data is then used to calibrate the \mathcal{GP} model and generate new plausible contour samples. The latter are finally used to analyze the probability density function (PDF) of the local fiber volume fraction V_f of the fiber tow.

Program 1: Methodology for stochastic characterization of fiber tows.

Input: *tomogram*

Parameters: parameters for Alg. 1, Alg. 3, and Alg. 2

- 1 extract $P_p(x, y)$, $P_s(x, y)$ and $\hat{\Gamma}^{init}$ after [16]
- 2 data preprocessing with Alg. 3;
- 3 calibrate kernel with Alg. 2;
- 4 sample new contours with Alg. 1;
- 5 calculate V_f for each contour (Eq. (22));
- 6 return the PDF of V_f ;

5.1. Material and data acquisition

The material used in the study is a composite of a vinyl-ester matrix reinforced with three plies of TG96N60E glass fiber textile provided by *Texonic*[26]. The textile has a 3D orthogonal fabric architecture with unidirectional tows (non-crimp) placed in the warp and weft directions, kept together by a binder yarn. The composite was manufactured by Resin Transfer Molding (RTM). The liquid resin was injected at a constant rate into dry fibrous reinforcement placed in a rigid metallic mold. The intended fiber weight fraction was 50%. The scanned sample was cut from the center of the manufactured specimen (Fig. 8) and had

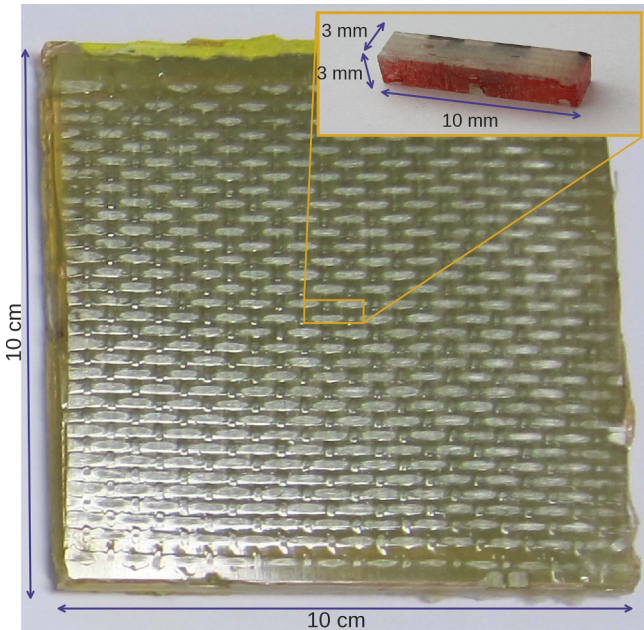


Fig. 8. Geometry of the composite specimen and location of the sample used in the microtomographic study.

Table 1

Parameters of data acquisition with X-ray microtomography.

Parameter	Value
Acceleration voltage	80 kV
Beam current	280 μ A
No. of projections	1500
Scan resolution	3.0 μ m

nominal dimensions of 3x3x10 mm. The scans were realized at Laboratoire Mateis of INSA de Lyon, France on a vtomex X-ray microtomograph with parameters of acquisition detailed in Table 1.

The radiographic projections were reconstructed with the filtered back-projection algorithm [27] into tomograms. One volume consisted of 1200 reconstructed slices requiring 1.5 GB of memory. It provided information on ten fiber tows, from which a single tow was selected and an example tomogram was subject to stochastic characterization.

5.2. Data preprocessing

The reconstructed tomogram is subject to two types of segmentation with Fast Random Forest learning algorithms as in [16]. Firstly, the phase segmentation is performed yielding phase probability $P_p(x, y)$ (Fig. 1b) from which ϕ and vol_{fb} are further determined. Secondly, a structure segmentation is realized giving $P_s(x, y)$ (Fig. 1c) and the initial contour $\hat{\Gamma}^{init}$ discretized with t^0 . The discrete values of $P_s(x, y)$ are stored as a matrix $\mathbb{P}_{N \times M}$ where N and M are respectively the width and height of the tomographic image and

$$\hat{\Gamma}^{init} = \begin{bmatrix} i_1 & \dots & i_{n_t^0} \\ j_1 & \dots & j_{n_t^0} \end{bmatrix} \quad (18)$$

is a set of indexes in \mathbb{P} . From this data we identify the probability P_c of a contour and its mean coordinates (x^0, y^0) and variances $\sigma_{x^0}^2, \sigma_{y^0}^2$ to construct the stochastic model. The operations enabling this identification are summarized in Alg.3 presented in Appendix B. The coordinates (x_i^0, y_i^0) are equivalent to the expected value of P_c (Fig. 9) in the subregion ω_i of size $l \times l$

$$x_i^0 = \frac{\int_{\omega_i} P_c(x, y)x d\omega_i}{\int_{\omega_i} P_c(x, y) d\omega_i}, \quad i = 1, \dots, n_t^0 \quad (19)$$

with the variance

$$\sigma_{x_i^0}^2 = \frac{\int_{\omega_i} P_c(x, y)(x - x_0)^2 d\omega_i}{\int_{\omega_i} P_c(x, y) d\omega_i}, \quad i = 1, \dots, n_t^0. \quad (20)$$

The integration is analogous for y_i^0 and $\sigma_{y_i^0}^2$. In the algorithm, this operation is performed by convolving data matrices with a $l \times l$ all-ones matrix filter J (Alg. 3 lines 6–14)

$$J = \mathbb{1}_l \mathbb{1}_l^T. \quad (21)$$

The choice of l depends on the resolution of the scan. For high resolutions, larger values of l reduce the impact of local disturbances introduced by the individual fibers. Smaller values of l are more adequate for low resolutions to maintain the detail of tow contour



Fig. 9. Contour probability $P_c(x, y)$ obtained from $P_s(x, y)$. The result has been scaled in the 0–1 range.

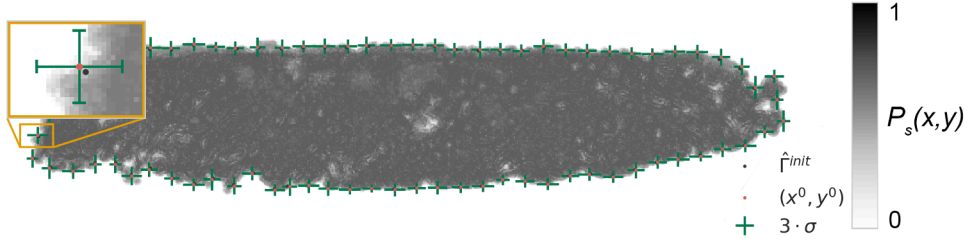
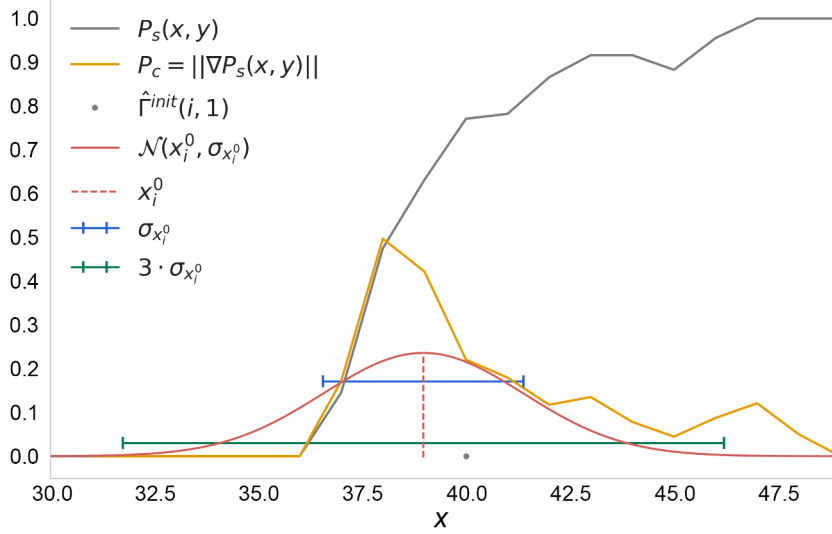

(a) P_s overlaid with $\hat{\Gamma}^{init}$, (x^0, y^0) and $3 \cdot \sigma$.

(b) Comparison between P_s and P_c for the point shown in the inset of (a).

Fig. 10. Points (x^0, y^0) identified after evaluating P_c from P_s data: (a) P_s overlaid with $\hat{\Gamma}^{init}$, (x^0, y^0) and $3 \cdot \sigma_{x^0}$, $3 \cdot \sigma_{y^0}$; (b) P_s and P_c for the point shown in the inset of (a).

geometry.

The points (x^0, y^0) are shown in Fig. 10a compared with the initial indexes $\hat{\Gamma}^{init}$. The new coordinates (Fig. 10b) are closer to the peak of P_c , while the initial identification remains within the error of measurement.

The data obtained during the preprocessing step are summarized in Table 2. The discretization of (x^0, y^0) can be further adjusted through filtering by curvature energy as in [28], thus reducing the computational load.

5.3. Fitting of the model

The preprocessing step has yielded data required to build and calibrate the stochastic model. The $\mathcal{G}\mathcal{P}$ is defined by the periodic kernel (Eq. (11)) and the mean function (Eq. (9)) is considered constant $\mu_x(t) = \mu_y(t) \equiv 0$ without loss of generality. The influence of θ and α has been studied in Fig. 11. It can be observed that for higher values of θ , the perimeter of the tow contour tends to a stable value, characteristic for the smooth reconstruction, similar to the one shown in Fig. 12a. At the same time, the area of volume cross-section f_3 exhibits multiple

local minima in function of θ , with increasing variability for higher values of α . For larger values of θ , the area encompassed by the contour diminishes beyond that of the original reconstruction (Fig. 12b).

This decrease in area also translates into a loss of the total area f_1 of cross-sections of individual fibers contained within the contour. The graph of f_1 within 3σ confidence intervals (Fig. 13) in function of θ shows that while the increase of the upper bounds of the contour (Fig. 13b) results in a marginal increase of the cross-sectional area of fibers included within the contour, for the lower bound (Fig. 13a) the difference between the target total fiber area vol_{fib} and that obtained becomes substantial. For high values of α , such as 0.05, even 16% of fibers are left out of the reconstructed contour.

5.4. Stochastic characterization of V_f

Once the kernel function is calibrated, we may proceed to the Monte Carlo sampling of plausible contours (Alg. 1). An example of such sampling is shown in Fig. 14. These samples are now used to determine the local fiber volume fraction V_f of a tow. The V_f is defined as the ratio of the volume of fibers to the volume of a fiber tow, which in a 2D case is equivalent to

$$V_f = \frac{\text{volume}_{\text{fibers}}}{\text{volume}_{\text{tow}}} = \frac{\int_{\Omega(\Theta)} \phi(x, y) d\Omega(\Theta)}{f_3}. \quad (22)$$

Fig. 15 shows two PDF fitted to histograms of distribution of V_f obtained from 5000 contours sampled from the calibrated GP model. The first distribution (Fig. 15a) resulted from the model sampled with $\alpha = 0.2$. The mean of GP and of the samples differed only by 1.5% from the value of V_f identified in the initial deterministic segmentation. Knowing that the initial segmentation was not optimal, we augmented α to 2.5, yielding a new mean 4% lower than the initial V_f (Fig. 15b).

Table 2
Input data for reconstruction of one tow contour.

Data	No. of points
$P_p(x, y)$	$8.89 \cdot 10^5$
where $P_p(x, y) \geq 0.5$	$3.01 \cdot 10^5$
$P_s(x, y)$	$8.89 \cdot 10^5$
(x^0, y^0)	Before filtering $4.67 \cdot 10^3$
	After filtering $1.66 \cdot 10^3$

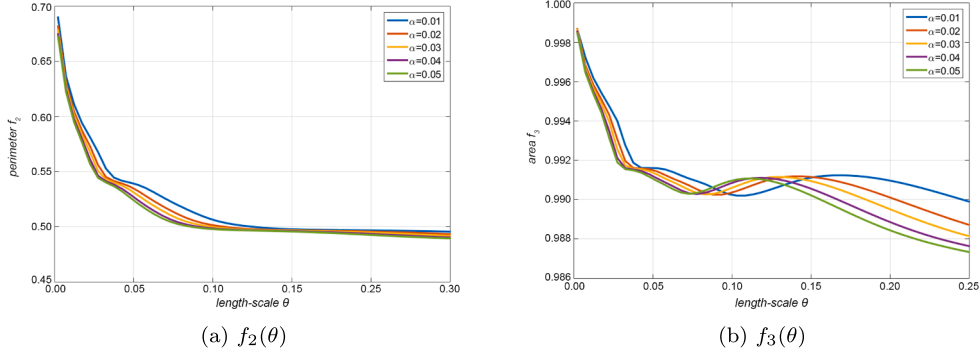


Fig. 11. Influence of θ and α on (a) f_2 (contour perimeter) and (b) f_3 (tow area) for the contour extracted from X-ray microtomographic data. The values of f_2 and f_3 are scaled to the 0–1 range.

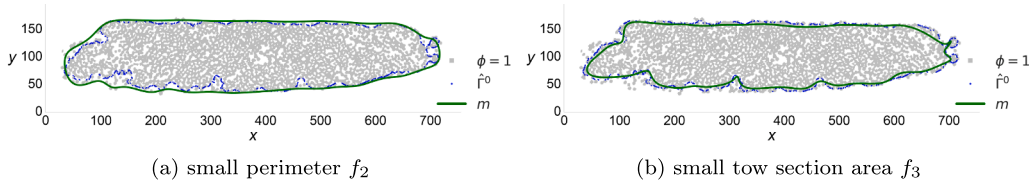


Fig. 12. Admissible solutions for (a) small perimeter f_2 (b) small tow section area f_3 .

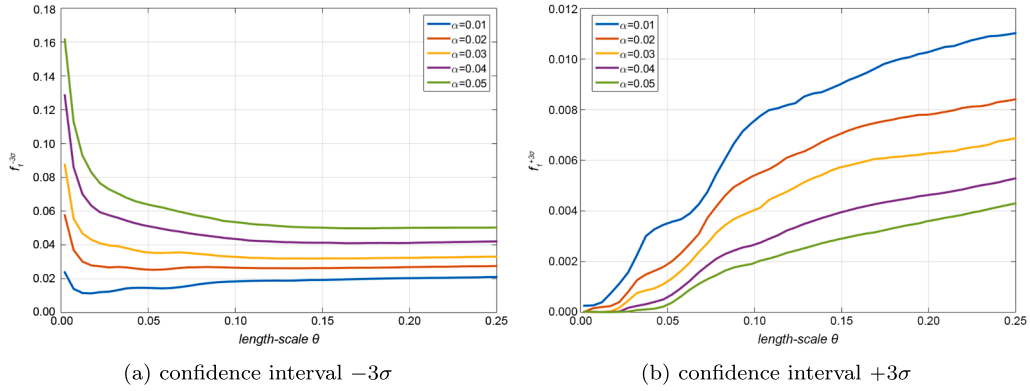


Fig. 13. Error in fiber volume f_1 with respect to vol_{fib} for different α within confidence intervals (a) -3σ ; (b) $+3\sigma$. Please note that the scale in (a) and (b) differs by one order of magnitude.

The reason for these discrepancies can be identified by investigating sampled contours in Fig. 14b. The increase in α leads to the inclusion of individual fibers around the fiber tow. Even though the area of fiber cross-sections increases marginally (Fig. 13b), the inclusion of individual fibers surrounded by pure resin or air results in the lower V_f . Less variation in $\alpha\sigma$ leads to less variation in the inclusion of fibers and thus the identified V_f is closer to the one resulting from deterministic measurement. It may be concluded, that the use of higher values of α is

of value when a calibration of the segmentation process is required. On the other hand, once calibrated, the smaller α would ensure less noise in the stochastic identification of V_f .

It can be observed that some fibers belonging to the tow may be beyond the reach of the generated samples. Thus a reconstruction with low α may lead to the omission of single fibers around the contour and surrounded by resin giving a higher V_f . Larger α increases the probability of inclusion of such “floating fibers” in the contour, and

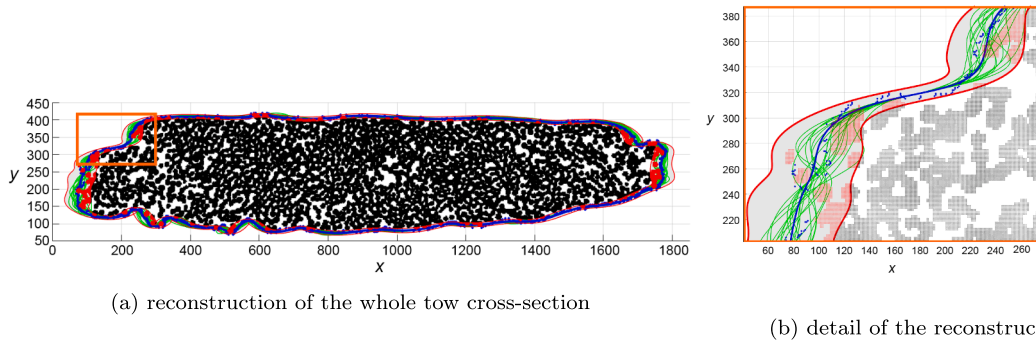


Fig. 14. Sampling (green) of \mathcal{S} superimposed over the results of phase segmentation (black). The mean of \mathcal{S} is marked in blue and $\pm 3\sigma$ confidence interval is marked in red. For references to color please refer to the online version of this paper.

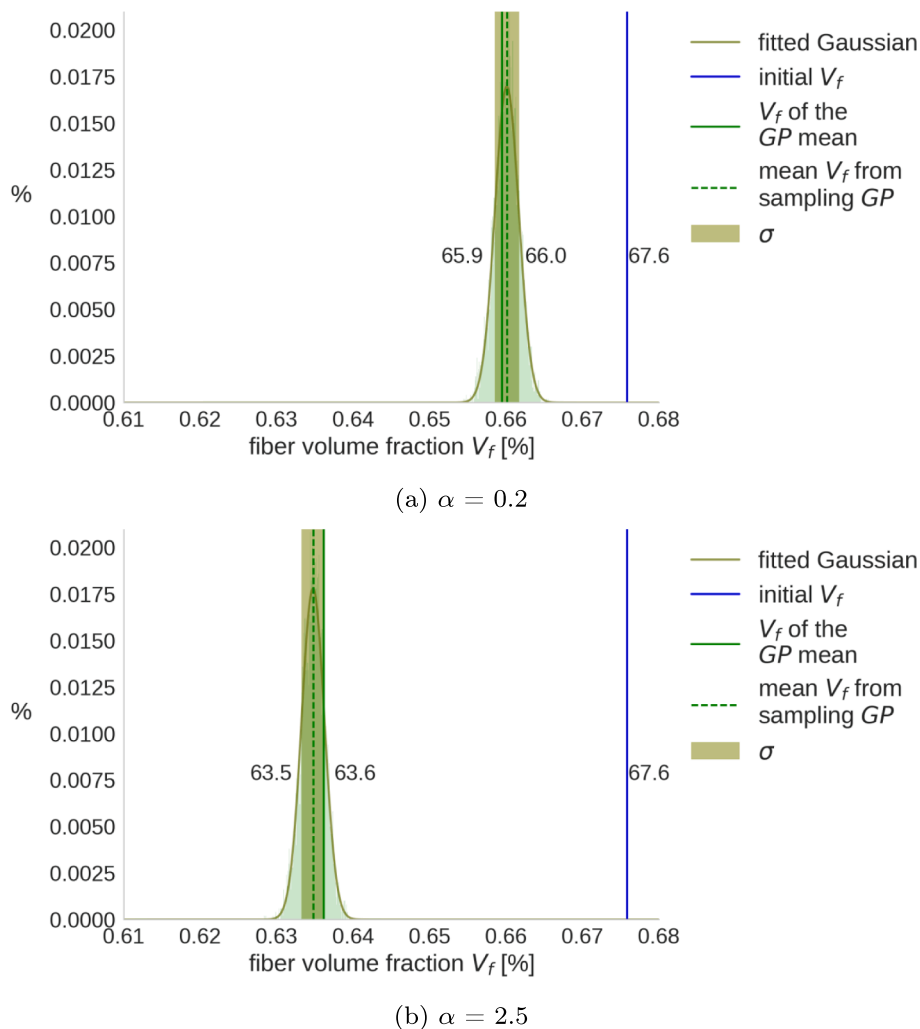


Fig. 15. Distribution of V_f for different error strength factors (a) $\alpha = 0.2$ (b) $\alpha = 2.5$. Here, the σ relates to the distribution of V_f .

consequently also of the surrounding resin, resulting in lower V_f . These two cases are illustrated in Fig. 15, where the V_f values of samples are approximated by a Gaussian distribution with a spread of values from 63% (all “floating fibers” included) to 64% (only the core of the fiber tow with smooth geometry).

5.5. Computational aspects

The whole procedure outlined in Program 1 for one cross-section took 3 min on 8×2.80 GH CPU Intel® Core™ i7-7700HQ processors. The matrix operations (convolutions and Hadamard product, division and root) in Alg.3, image segmentation and calculation of f_1 , f_2 , f_3 were programmed with the help of *Python OpenCV* library [29] for calculations on Graphics Processing Units (GPU) and executed on NVIDIA® GeForce® GTX 1060. After parallelization and adjustment of parameters of Alg.2 the total execution time was decreased to 22.5 s. Despite that, with the amount of data averaging 1.5 GB per scan, further optimization is necessary to perform the reconstruction of the microstructure of the entire specimen. Three solutions can be proposed to decrease the computational load. The first approach is to perform complete optimization on chosen cross-sections and optimization on constrained parameters for the intermediate ones. The second solution relies on the filtering of cross-sections to retrieve only the shapes which differ significantly and interpolating the rest. The choice depends on the intended application of the geometry as well as on the type of textile architecture. Three-dimensional textiles composed of different types of

fibers would certainly benefit from the latter. Another solution consists of employing a better performing approach to optimize the hyperparameters.

6. Conclusions

We have presented a method to generate sets of plausible geometries of a textile reinforcement in composites from X-ray microtomographic scans. We have formulated a stochastic solution using the Gaussian Process underlying the deterministic kriging model. The advantages of this formulation are multiple. First of all, during model calibration, two extreme types of reconstruction are obtained: smooth, adequate for generation of a simplified mesh for Finite Element Analysis; and a detailed one, interesting for prediction of microscale permeability. The intermediate solution can be used to characterize local material characteristics such as fiber volume fraction V_f . We have observed, that the mean V_f obtained from the stochastic model differed significantly from the one based on the deterministic reconstruction. For structural applications where larger specimens need to be investigated, high resolution scans may not be possible, either due to X-ray scanner limitations and/or data processing costs. In such case, the presented method can be first calibrated with high resolution data from another imaging technique, such as Scanning Electron Microscopy, and then reused for low-resolution X-ray microtomographic scans.

When treating microtomographic scans of compressed textiles, special care must be taken to avoid intersections of neighboring tows,

for example by introducing another constraint. The methodology presented here can be also extended to three-dimensional geometry. These two issues are the subject of an ongoing study.

Data availability

The raw/processed data required to reproduce these findings cannot be shared at this time as the data also forms part of an ongoing study.

Appendix A. Appendix A

The flow of the optimization algorithm is shown in Alg.2 below. The optimization begins by generating a random population of kernel hyperparameters with which a contour is fitted to the (x^0, y^0) and objective functions are evaluated. Following a ranking of hyperparameter sets according to the dominance criterion, a new population is generated by crossover, mutation and niching. The choice of algorithm parameters is adapted empirically depending on the quality of the initial segmentation, with good initial approximations requiring less generations to provide satisfactory results.

Algorithm 2: Kernel calibration with NSGA-II algorithm.

Input	: $x^0, y^0, t^0, t^*, \alpha$, kernel function (Eq. 11), σ_x^2, σ_y^2
Parameters	: number of generations G , population size g , crossover rate, mutation rate, niching distance

```

1 generate a population of  $g$  random  $\Theta$ ;
2 for 1 to  $G$  generations do
3   for each  $\Theta$  in population do
4     compute  $C$  (Eq. 8);
5     invert  $C^{00}$ ;
6     calculate  $m_x$  (Eq. 6) and  $m_y$ ;
7     approximate  $f_1$  by the sum of voxel values
        $\phi(x_i, y_i), x_i, y_i \in \Omega(\Theta)$ ;
8     approximate  $f_2$  by the sum of distances
        $\sum_{i=1}^{n_i^*} [(x(t_{i+1}^* - x(t_i^*)))^2 + (y(t_{i+1}^* - y(t_i^*)))^2]^{\frac{1}{2}}$ ;
9     approximate  $f_3$  by the voxel count  $x_i, y_j \in \Omega(\Theta)$ ;
10  end
11  rank individuals according to the dominance criterion;
12  create new population by crossover, mutation, niching;
13 end
14 return the Pareto set of non-dominated  $\Theta$  from the last generation;
```

Appendix B. Appendix B

The probability P_c of the contour can be determined by analyzing the gradient of P_c

$$P_c(x, y) = \|\nabla P_c(x, y)\| = \sqrt{\left(\frac{\partial P_c(x, y)}{\partial x}\right)^2 + \left(\frac{\partial P_c(x, y)}{\partial y}\right)^2}. \quad (23)$$

For the discrete representation \mathbb{P} , the partial derivatives can be approximated by convolution (Alg.3 lines 1–2) with directional Sobel filters

$$S_x = \begin{bmatrix} 1 & 0 & -1 \\ 2 & 0 & -2 \\ 1 & 0 & -1 \end{bmatrix} = \begin{bmatrix} 1 \\ 2 \\ 1 \end{bmatrix} [1 \ 0 \ -1], \quad S_y = \begin{bmatrix} 1 & 2 & 1 \\ 0 & 0 & 0 \\ -1 & -2 & -1 \end{bmatrix} = \begin{bmatrix} 1 \\ 0 \\ -1 \end{bmatrix} [1 \ 2 \ 1] \quad (24)$$

resulting in images Fig. 16a and b. Then, the discrete P_c (Alg.3 line 3) will be as in Fig. 9.

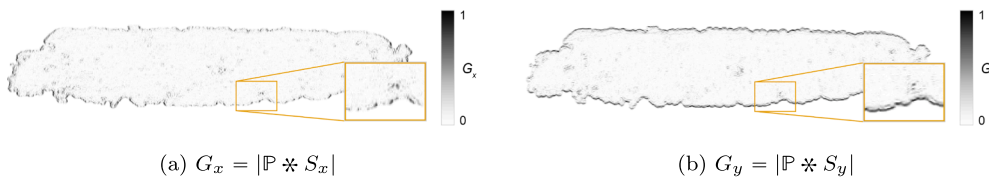


Fig. 16. Results of the convolution of $P_c(x, y)$ with the Sobel filter (Eq. (24)): (a) in the x-direction; (b) in the y-direction. The absolute value of the result has been scaled in the 0–1 range. Higher intensity indicates larger value of the derivative.

Algorithm 3: Identification of (x^0, y^0) and $\sigma_{x^0}^2, \sigma_{y^0}^2$ from $\mathbb{R}(x, y)$.

Input : $\mathbb{P}_{N \times M}, \mathbb{X} = (x_1, \dots, x_N)^T, \mathbb{Y} = (y_1, \dots, y_M)^T,$
 $\hat{\Gamma}^{init}, n_{\theta^0}$

Parameters : filters S_x, S_y, J

Matrix operators: convolution \ast , Hadamard: multiplication \odot ,
 root $\circ_{\frac{1}{2}}$, division \oslash

1 $G_x = |\mathbb{P} \ast S_x|;$
 2 $G_y = |\mathbb{P} \ast S_y|;$
 3 $P_c = (G_x \odot G_x + G_y \odot G_y) \circ_{\frac{1}{2}}$ (Eq. 23);
 4 $\mathbb{X} = \mathbb{1}_{N \times 1} \mathbb{X}^T;$
 5 $\mathbb{Y} = \mathbb{y} \mathbb{1}_{M \times 1}^T;$
 6 $\mathbb{M}_x = (P_c \odot \mathbb{X}) \ast J \oslash (P_c \ast J);$
 7 $\mathbb{M}_y = (P_c \odot \mathbb{Y}) \ast J \oslash (P_c \ast J);$
 8 $\Sigma_x^2 = (P_c \odot \mathbb{X} \odot \mathbb{X}) \ast J \oslash (P_c \ast J) - \mathbb{M}_x \odot \mathbb{M}_x;$
 9 $\Sigma_y^2 = (P_c \odot \mathbb{Y} \odot \mathbb{Y}) \ast J \oslash (P_c \ast J) - \mathbb{M}_y \odot \mathbb{M}_y;$
 10 **for** $i = 1$ **to** n_{θ^0} **do**
 11 $x_i^0 = \mathbb{M}_x(\hat{\Gamma}^{init}(i, 1), \hat{\Gamma}^{init}(i, 2))$ (Eq. 19);
 12 $y_i^0 = \mathbb{M}_y(\hat{\Gamma}^{init}(i, 1), \hat{\Gamma}^{init}(i, 2));$
 13 $\sigma_{x_i^0}^2 = \Sigma_x^2(\hat{\Gamma}^{init}(i, 1), \hat{\Gamma}^{init}(i, 2))$ (Eq. 20);
 14 $\sigma_{y_i^0}^2 = \Sigma_y^2(\hat{\Gamma}^{init}(i, 1), \hat{\Gamma}^{init}(i, 2));$
 15 **end**
 16 **return** coordinates (x^0, y^0) and errors $\sigma_{x^0}^2, \sigma_{y^0}^2$;

References

- [1] Azaiez J, Chiba K, Chinesta F, Poitou A. State-of-the-art on numerical simulation of fiber-reinforced thermoplastic forming processes. *Arch Comput Methods Eng* 2002;9(2):141–98. <https://doi.org/10.1007/BF02736650>.
- [2] García JA, Gascón L, Chinesta F. A fixed mesh numerical method for modelling the flow in liquid composites moulding processes using a volume of fluid technique. *Comput Methods Appl Mech Eng* 2003;192:877–93. [https://doi.org/10.1016/S0045-7825\(02\)00604-7](https://doi.org/10.1016/S0045-7825(02)00604-7).
- [3] García J, Gascón L, Cueto E, Ordeig I, Chinesta F. Meshless methods with application to Liquid Composite Molding simulation. *Comput Methods Appl Mech Eng* 2009;198(33–36):2700–9. <https://doi.org/10.1016/j.cma.2009.03.010>.
- [4] Devalve C, Pitchumani R. Simulation of void formation in liquid composite molding processes. *Compos Part A: Appl Sci Manuf* 2013;51:22–32. <https://doi.org/10.1016/j.compositesa.2013.03.016>.
- [5] Naouar N, Vidal-Sallé E, Schneider J, Maire E, Boisse P. 3D composite reinforcement meso F.E. analyses based on X-ray computed tomography. *Compos Struct* 2015;132:1094–104. doi:10.1016/j.compstruct.2015.07.005.
- [6] Niknezhad D, Raghavan B, Bernard F, Kamali-bernard S. Towards a realistic morphological model for the meso-scale mechanical and transport behavior of cementitious composites. *Compos Part B* 2015;81:72–83. <https://doi.org/10.1016/j.compositesb.2015.06.024>.
- [7] Durville D, Baydoun I, Wielhorski Y. Determining the initial configuration and characterizing the mechanical properties of 3D angle-interlock fabrics using finite element simulation. *Int J Solids Struct* 2018. <https://doi.org/10.1016/j.ijsolstr.2017.06.026>.
- [8] Shinoda T, Odani H, Wadahara E. A-vartm technology application for Japan's new regional jet aircraft. 16th International Conference on Composite Materials. 2007. p. 1–9.
- [9] Vanaerschot A, Panerai F, Cassell A, Lomov SV, Vandepitte D, Mansour NN. Stochastic characterisation methodology for 3-D textiles based on micro-tomography. *Compos Struct* 2017;173:44–52. <https://doi.org/10.1016/j.compstruct.2017.03.107>.
- [10] LeBel F. Contrôle De La Fabrication Des Composites Par Injection Sur Renforts. Université de Montréal 2012. [Ph.D. thesis].
- [11] Somashekar AA, Bickerton S, Bhattacharyya D. Compression deformation of a biaxial stitched glass fibre reinforcement: visualisation and image analysis using X-ray micro-CT. *Compos Part A: Appl Sci Manuf* 2011;42(2):140–50. <https://doi.org/10.1016/j.compositesa.2010.10.017>.
- [12] Naouar N, Vidal-Sallé E, Schneider J, Maire E, Boisse P, Vidal-Sallé E, Schneider J, Maire E, Boisse P. Meso-scale FE analyses of textile composite reinforcement deformation based on X-ray computed tomography. *Compos Struct* 2014;116(1):165–76. <https://doi.org/10.1016/j.compstruct.2014.04.026>.
- [13] Neves AA, Jacques S, Van Ende A, Cardoso MV, Coutinho E, Lührs AK, Zicari F, Van Meerbeek B. 3D-microleakage assessment of adhesive interfaces: exploratory findings by micro-CT. *Dent Mater* 2014;30(8):799–807. <https://doi.org/10.1016/j.dental.2014.05.003>.
- [14] Rolland H, Saintier N, Robert G. Damage mechanisms in short glass fibre reinforced thermoplastic during in situ microtomography tensile tests. *Compos Part B: Eng* 2016;90:365–77. <https://doi.org/10.1016/j.compositesb.2015.12.021>.
- [15] Hassan MH, Othman AR. Contribution of processing parameters on void content in the vacuum bagging configurations of L-shaped composite laminates. *Int J Adv Manuf Technol* 2017. <https://doi.org/10.1007/s00170-017-0585-6>.
- [16] Madra A, Breitkopf P, Rassinoux A, Trochu F. Image-based model reconstruction and meshing of woven reinforcements in composites. *Int J Numer Meth Eng* 2017.
- [17] Aravand MA, Shishkina O, Straumit I, Liotta AH, Wicks SS, Wardle BL, Lomov SV, Gorbatikh L. Internal geometry of woven composite laminates with fuzzy carbon nanotube grafted fibers. *Compos Part A: Appl Sci Manuf* 2016;88:295–304. <https://doi.org/10.1016/j.compositesa.2016.06.010>.
- [18] Yousaf Z, Potluri P, Withers P, Mollenhauer D, Zhou E, Duning S. Digital element simulation of aligned tows during compaction validated by computed tomography (CT). *Int J Solids Struct* 2017;1–10. <https://doi.org/10.1016/j.ijsolstr.2017.05.044>. <http://linkinghub.elsevier.com/retrieve/pii/S0020768317302755>.
- [19] Lê M, Unkelbach J, Ayache N, Delingette H. Sampling image segmentations for uncertainty quantification. *Med Image Anal* 2016;34:42–51. <https://doi.org/10.1016/j.media.2016.04.005>.
- [20] Roy S, Bandyopadhyay SK. A new method of brain tissues segmentation from MRI with accuracy estimation. *Proc Comput Sci* 2016;85(Cms):362–9. <https://doi.org/10.1016/j.procs.2016.05.244>.
- [21] Cruz-Aceves I, Oloumi F, Rangayyan RM, Avina-Cervantes JG, Hernandez-Aguirre A. Automatic segmentation of coronary arteries using Gabor filters and thresholding based on multiobjective optimization. *Biomed Signal Process Control* 2016;25:76–85. <https://doi.org/10.1016/j.bspc.2015.11.001>.
- [22] Mertens A, Simar A, Adrien J, Maire E, Montrieux HM, Delannay F, Lecomte-Beckers J. Influence of fibre distribution and grain size on the mechanical behaviour of friction stir processed Mg-C composites. *Mater Charact* 2015;107:125–33. <https://doi.org/10.1016/j.matchar.2015.07.010>.
- [23] Ripley BD. *Stochastic simulation*. New York: Wiley; 1987.
- [24] Rasmussen CE, Williams CKI. *Gaussian processes for machine learning*. Boston: MIT Press; 2006. arXiv:026218253X, doi:10.1142/S0129065704001899.
- [25] Deb K, Pratap A, Agarwal S, Meyarivan T. A fast and elitist multiobjective genetic algorithm: NSGA-II. *IEEE Trans Evol Comput* 2002;6(2):182–97. <https://doi.org/10.1109/4235.996017>.
- [26] Texonic; 2017. <http://texonic.net/>.
- [27] Dudgeon DE, Mersereau RM. *Multidimensional Digital Signal Processing*. Prentice Hall; 1984.
- [28] Cruchaga M, Celentano D, Breitkopf P, Villon P, Rassinoux A. A front remeshing technique for a Lagrangian description of moving interfaces in two-fluid flows. *Int J Numer Meth Eng* 2006;66(13):2035–63. <https://doi.org/10.1002/nme.1616>.
- [29] Itseez. Open source computer vision library; 2017. <https://github.com/itseez/opencv>.